Li$_2$O-Based Cathode Additives Enabling Prelithiation of Si Anodes

Yeyoung Ha [1],*, Maxwell C. Schulze [1], Sarah Frisco [1], Stephen E. Trask [2], Glenn Teeter [1], Nathan R. Neale [1], Gabriel M. Veith [3] and Christopher S. Johnson [2],*

[1]   Materials, Chemical, and Computational Science Directorate, National Renewable Energy Laboratory, 15013 Denver West Parkway, Golden, CO 80401, USA; Max.Schulze@nrel.gov (M.C.S.); Sarah.Frisco@nrel.gov (S.F.); Glenn.Teeter@nrel.gov (G.T.); Nathan.Neale@nrel.gov (N.R.N.)

[2]   Argonne National Laboratory, Chemical Sciences and Engineering Division, 9700 South Cass Avenue, Lemont, IL 60439, USA; trask@anl.gov

[3]   Oak Ridge National Laboratory, Materials Science and Technology Division, Oak Ridge, TN 37831, USA; veithgm@ornl.gov

*   Correspondence: Yeyoung.Ha@nrel.gov (Y.H.); cjohnson@anl.gov (C.S.J.)

Abstract: Low first-cycle Coulombic efficiency is especially poor for silicon (Si)-based anodes due to the high surface area of the Si-active material and extensive electrolyte decomposition during the initial cycles forming the solid electrolyte interphase (SEI). Therefore, developing successful prelithiation methods will greatly benefit the development of lithium-ion batteries (LiBs) utilizing Si anodes. In pursuit of this goal, in this study, lithium oxide (Li$_2$O) was added to a LiNi$_{0.6}$Mn$_{0.2}$Co$_{0.2}$O$_2$ (NMC622) cathode using a scalable ball-milling approach to compensate for the initial Li loss at the anode. Different milling conditions were tested to evaluate the impact of particle morphology on the additive performance. In addition, Co$_3$O$_4$, a well-known oxygen evolution reaction catalyst, was introduced to facilitate the activation of Li$_2$O. The Li$_2$O + Co$_3$O$_4$ additives successfully delivered an additional capacity of 1116 mAh/g$_{Li2O}$ when charged up to 4.3 V in half cells and 1035 mAh/g$_{Li2O}$ when charged up to 4.1 V in full cells using Si anodes.

Keywords: lithium-ion batteries; silicon anodes; prelithiation; cathode additives; lithium oxide; cobalt oxide

1. Introduction

Silicon (Si) is a promising next-generation anode material for lithium (Li)-ion batteries (LiBs) owing to its high theoretical specific capacity (3579 mAh/g upon formation of Li$_{15}$Si$_4$) and relatively low operating voltage (~0.4 V vs. Li/Li$^+$) [1–3]. Its alloying chemistry, however, results in large volume change (~280%) during operation, which leads to pulverization and loss of active material. To mitigate the mechanical failure of electrodes, Si is typically utilized as nanometer-sized particles [4,5]. Such small particles, however, create extremely high surface area and, as a result, Si-based electrodes suffer from significant Li consumption during the formation of the solid electrolyte interphase (SEI) in the initial cycles.

One possible solution to this problem is supplying excess Li in the system, i.e., prelithiation, to compensate for the initial loss [6–8]. For example, additional Li can be chemically incorporated into Si anodes by immersing the electrode in reactive agent solutions such as Li-reduced polyaromatics [9,10] or bringing it into direct contact with Li metal [11,12]. Alternatively, Si anodes can be electrochemically prelithiated by cycling the electrode in an electrochemical cell using Li metal counter electrode [13,14]. These methods supply Li to the anode, and this additional Li can compensate for the loss during the initial charge by providing sufficient capacity during the reverse (discharge) cycle. Alternatively, additional Li can be introduced to the cathode to provide the capacity required for the SEI formation. For example, the cathode-active material can be over-lithiated via chemical or

electrochemical processes [15,16], or additives capable of releasing Li during charge can be incorporated [17–25].

Among these methods, utilizing cathode additives is a convenient approach, as it does not require an additional step in the battery-manufacturing process (the additives can be directly incorporated into the cathode slurry) nor a complicated synthetic process to alter the cathode-active materials. Different additives, such as lithium nitride (Li_3N) [17,18], anti-fluorite Li_5FeO_4 (LFO) [19,20], lithium sulfide (Li_2S), [21,22], and lithium oxide (Li_2O) [23–25] have been explored. While all these additives have shown promise, the chemical instability of Li_3N, LFO, and Li_2S brings challenges. Li_2O is a safe, cost-effective candidate that can release Li^+ during the first charge half-cycle and remain inactive in the following cycles, due to the large hysteresis of the reverse reaction [23,24]. However, since Li_2O is electrically insulating, activating this material and obtaining the additional capacity provided by this Li^+ source are nontrivial.

Previous work by Sun et al. showed nanocomposites of Li_2O and Co created by reacting Co_3O_4 with molten Li metal can deliver additional capacities at voltages below 4.1 V vs. Li/Li^+ upon charging [23]. In addition, Abouimrane et al. utilized ball-milled, micro-sized Li_2O powder and demonstrated that the additive performance depends on the charging rate, electrolyte, and the anode [24]. Recently, Qiao et al. reported anode-free Li-metal batteries where the cathode ($LiNi_{0.8}Co_{0.1}Mn_{0.1}O_2$) was coated with Li_2O, and fluorinated ether electrolyte additive was used to create a lithium fluoride (LiF)-rich cathode electrolyte interface (CEI), suppressing reactions between O_2^- species and the electrolyte [25]. Thus, there is a clear trend of growing interest in utilizing Li_2O as a cathode additive for prelithiation.

In this work, we evaluated how to effectively utilize the cathode Li_2O additive, specifically for prelithiating Si anodes. The impact of Li_2O particle size and the presence of Co_3O_4 catalyst on the additive performance was systematically examined. Co_3O_4 is a well-known catalyst for oxygen evolution reaction (OER) at the cathode of Li-air batteries [26–28]; the oxidation of Li_2O is similar to charging Li-air batteries. Thus, Co_3O_4 is added to serve as an electrocatalyst to induce OER by coating the Li_2O particle surface. While there are different approaches to preparing and incorporating the additives into the cathode, here, we focused on the scalability of the method by implementing a simple high-energy ball-milling process under ambient conditions. The additives were added to the $LiNi_{0.6}Mn_{0.2}Co_{0.2}O_2$ (NMC622) cathode and the additive-containing electrode performance was tested in half cells and full cells using Si anodes. We discussed the limitations of these additives and propose the next steps toward developing successful Li_2O-based additives for high energy density LiBs.

2. Materials and Methods

2.1. Additive Preparation

Li_2O (97%, –60 mesh, Sigma-Aldrich, St. Louis, MO, USA) additives were prepared via three different methods: (1) planetary milling for 1100 rpm for 5 min; (2) planetary milling for 400 rpm for 1 h; and (3) planetary milling for 400 rpm for 1 h with Co_3O_4 additive (<1 μm, Sigma-Aldrich) in $3Li_2O + 1/3Co_3O_4$ stoichiometry. The 400 rpm for 1 h milling was performed in 15 min intervals, reversing the direction after each step. The milling process was performed in air, and the prepared powders were moved into a glove box for electrode fabrication.

2.2. Cathode Fabrication

The baseline NMC622 electrode was fabricated by mixing 90 wt % NMC622 powder (Ecopro BM, Cheongju-si, Korea), 5 wt % C45 conductive carbon (Timcal, Switzerland), and 5 wt % polyvinylidene fluoride (PVDF Solef 5130, Solvay) in N-methyl-2-pyrrolidinone (NMP, anhydrous, 99.5%, Sigma-Aldrich), and coating the slurry on a 20 μm thick aluminum (Al) foil. Electrodes with Li_2O additives contained 80 wt % of NMC622 and 10 wt % of the additive, with the rest of the parameters being the same. Slurry preparation and

electrode coating was performed inside an argon (Ar)-filled glove box. The electrodes had a ~10 mg/cm^2 loading and ~45 μm thickness excluding the current collector, and were dried at 120 °C under a vacuum prior to use.

2.3. Coin Cell Testing

The 2032-type coin cells were fabricated in an Ar-filled glove box. Half cells consisted of 15.5 mm diameter Li metal (99.9%, 0.75 mm thick, Alfa Aesar), 19 mm diameter Celgard 2325 separator, 14 mm diameter cathode, and 40 μL Gen2 electrolyte (1.2 M lithium hexafluorophosphate (LiPF$_6$) in ethylene carbonate (EC)/ethyl methyl carbonate (EMC) (3:7, *w/w*, Tomiyama Pure Chemical Industries, Ltd. (Tokyo, Japan)). Full cells consisted of 15 mm diameter Si anode, 19 mm diameter Celgard 2325 separator, 14 mm diameter cathode, and 40 μL Gen2 electrolyte. The Si electrode was provided by the Cell Analysis, Modeling and Prototyping (CAMP) Facility at Argonne National Laboratory. The anode was a mixture of 80 wt % Si (Paraclete Energy), 10 wt % C45 conductive carbon (Timcal), and 10 wt % lithium polyacrylate binder (LiPAA) mixture coated on a 10 μm thick copper (Cu) foil with a coating loading of 1.10 mg/cm^2 and thickness of 10 μm. The electrode exhibited 2.85 mAh/cm^2 during the first lithiation in a half cell with a 50 mV vs. Li/Li$^+$ cutoff voltage. The Si electrode was dried at 150 °C under vacuum and the Celgard 2325 separator was dried under a vacuum at room temperature prior to use.

Coin cells were cycled using a MACCOR Series 4000 Automated Test System. The cells were placed inside a MACCOR Model MTC-020 Temperature Chamber, which was set to 30 °C. A ~1.9 mA current was applied, which corresponded to a 1C rate for all cells. The same charge and discharge rates were applied without resting in between.

2.4. Surface Characterization

Scanning electron microscope (SEM) images of the additives were obtained with a Hitachi S-4800 microscope. The probe conditions of 3 kV acceleration voltage and 10 μA current were applied.
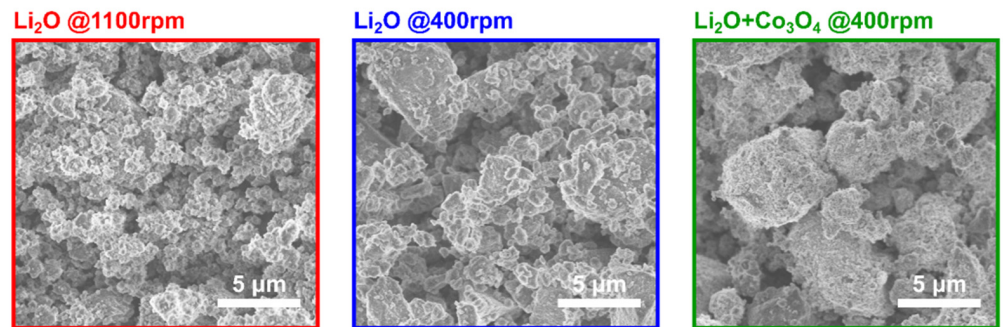
X-ray photoelectron spectroscopy (XPS) spectra were collected on a Physical Electronics 5600 XPS using Al-Kα excitation (hν = 1486.7 eV). Cycled electrodes were retrieved by disassembling coin cells in an Ar-filled glove box. The electrodes were soaked in 2 mL dimethyl carbonate (DMC) for 60 s to remove residual electrolyte and dried under dynamic vacuum at room temperature for 30 min. The electrodes were then sealed in an air-tight container and transferred to another Ar-filled glove box, which was connected to the XPS instrument. Samples were mounted in an Ar-filled glovebox and then brought into the XPS via a UHV transfer system, enabling analysis without exposure to atmosphere. The system had a base pressure above 2×10^{-9} Torr. Core level spectra were further analyzed using Igor Pro software [29].

3. Results and Discussion

3.1. Impact of Milling Conditions on the Additive Performance

SEM images of the three different Li$_2$O additives prepared via planetary ball-milling (two different milling conditions (1100 rpm for 5 min vs. 400 rpm for 1 h) and with and without the Co$_3$O$_4$ additive) are shown in Figure 1a. While all powders exhibited relatively wide particle size distribution, milling at higher revolutions per minute resulted in smaller particles with smoother edges (Li$_2$O @1100 rpm vs. Li$_2$O @400 rpm). When Co$_3$O$_4$ was added (Li$_2$O + Co$_3$O$_4$ @400 rpm), it coated the surface of Li$_2$O particles but did not seem to affect the milling process, as Li$_2$O + Co$_3$O$_4$ @400 rpm and Li$_2$O @400 rpm showed similar particle size and shape. Once the additives were incorporated into the electrode (Figure S1), they distributed evenly among the NMC622 particles, which were ~10 μm in diameter. The preparation method and performance of all additive-containing electrodes tested in this work are summarized in Table 1.

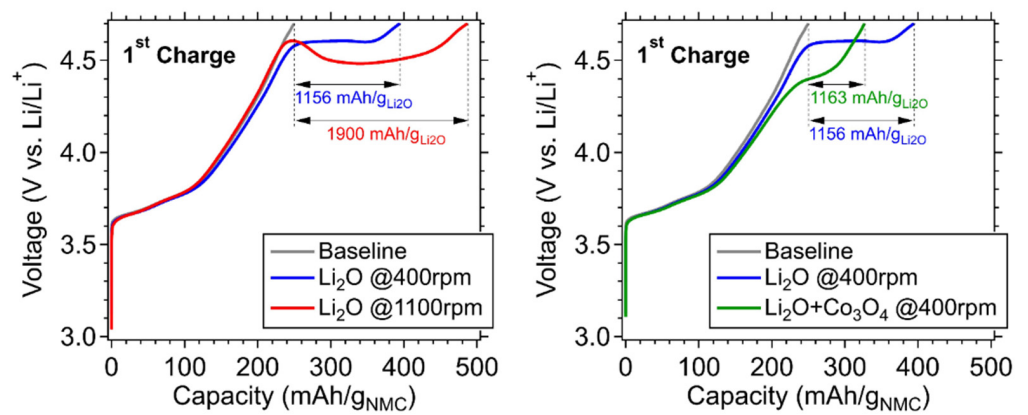**Figure 1.** (**a**) SEM images of additive powders and (**b**) half-cell voltage profiles of the additive-containing and baseline electrodes during the first charge. Half cells were charged at a C/20 rate up to 4.7 V at 30 °C. Voltage profiles are plotted as a function of grams of NMC in the electrode, excluding the mass of additives. Additional capacity obtained from the additives calculated per gram of Li_2O in the electrodes is indicated inside the figures for each profile.

Table 1. Summary of the electrodes examined in this work.

Electrode	Additive Composition	Milling Condition	Capacity (4.7 V vs. Li/Li^+)
Li_2O @400 pm	Li_2O	400 rpm for 1 h	1156 mAh/g_{Li2O}
Li_2O @1100 rpm	Li_2O	1100 rpm for 5 min	1900 mAh/g_{Li2O}
Li_2O + Co_3O_4 @400 rpm	$3Li_2O + 1/3Co_3O_4$	400 rpm for 1 h	1163 mAh/g_{Li2O} 614 mAh/$g_{Li2O+Co3O4}$
Li_2O + Co_3O_4 @1100 rpm	$3Li_2O + 1/3Co_3O_4$	1100 rpm for 5 min and 25 min rest, repeated 4 times	1504 mAh/g_{Li2O} 793 mAh/$g_{Li2O+Co3O4}$

Half-cell voltage profiles of the three Li_2O-containing electrodes and the baseline NMC622 electrode during the first charge are shown in Figure 1b. The cells were charged up to 4.7 V vs. Li/Li^+ and the profiles are plotted as a function of capacity per gram of NMC622 in the electrode. The same voltage profiles plotted as a function of mAh/cm^2 are shown in Figure S2. The additional capacity obtained from Li_2O is labeled for each electrode (mAh/g_{Li2O}). These values were calculated assuming 250 mAh/g from NMC622, which is an empirical value from the baseline electrode. First, comparing the baseline electrode and Li_2O @400 rpm, a plateau at ~4.6 V was observed for Li_2O @400 rpm, which corresponds to the reaction of Li_2O [24], and 1156 mAh/g_{Li2O} of additional capacity was obtained. When Li_2O was milled at higher revolutions per minute, i.e., Li_2O @1100 rpm, a greater capacity of 1900 mAh/g_{Li2O} was obtained. Both electrodes showed the activation of Li_2O starting at ~4.6 V vs. Li/Li^+, although the Li_2O @1100 rpm electrode showed

about a 100 mV decrease in the plateau as the reaction proceeded. We note the theoretical capacity of Li_2O, assuming its full conversion to $2Li^+ + 2e^- + \frac{1}{2}O_2$, is 1794 mAh/$g_{Li2O}$. The additional capacity obtained from the Li_2O @1100 rpm electrode (1900 mAh/g_{Li2O}) was larger than the theoretical value, indicating an inhomogeneous distribution of Li_2O particles and/or side reactions taking place along with the activation of Li_2O.

The addition of Co_3O_4 reduced this activation barrier and the $Li_2O + Co_3O_4$ @400 rpm electrode started to show additional capacity at ~4.35 V vs. Li/Li^+, demonstrating the catalytic activity of Co_3O_4. Although the additional capacity obtained from this electrode was smaller than that from the Li_2O @400 rpm electrode since the amount of Li_2O in the electrode was less (5.3 vs. 10 wt %), the capacity calculated per gram of Li_2O is 1163 mAh/g_{Li2O}, which is similar to that of the Li_2O @400 rpm electrode (1156 mAh/g_{Li2O}). Thus, these results indicate that the milling condition determines the utilization of Li_2O, where smaller particle size gives larger capacity per gram of Li_2O in the electrode, and the presence of Co_3O_4 lowers the overpotential for Li_2O activation. Based on these observations, we milled $Li_2O + Co_3O_4$ at 1100 rpm and tested the performance.

3.2. Performance of $Li_2O + Co_3O_4$ @1100 rpm Electrode

$Li_2O + Co_3O_4$ was planetary ball-milled at 1100 rpm for 5 min with a 25 min rest, and this sequence of steps was repeated four times. When added to the NMC622 electrode, these additives successfully delivered additional capacity at a voltage below 4.0 V in the half cells (Figure 2a). Note that the $Li_2O + Co_3O_4$ @400 rpm electrode showed additional capacity starting at ~4.35 V vs. Li/Li^+ (Figure 1b), demonstrating our approach of milling at higher revolutions per minute led to the enhanced performance of these additives. The charging profile of $Li_2O + Co_3O_4$ @1100 rpm exhibited a slope change at ~4.0 V, which appears as a distinct peak in the dQ/dV plot (Figure 2a inset). This feature corresponds to the plateau observed from the charging profiles of Li-O_2 batteries with Co_3O_4 catalyst [30,31]. The additional capacity obtained from $Li_2O + Co_3O_4$ @1100 rpm by charging up to 4.3 V vs. Li/Li^+ was 1116 mAh/g_{Li2O}, excluding the mass of Co_3O_4. Considering the total mass of both Li_2O and Co_3O_4, the additional capacity was 589 mAh/$g_{Li2O+Co3O4}$. The low activation voltage and considerable capacity obtained below 4.3 V vs. Li/Li^+ from this $Li_2O + Co_3O_4$ @1100 rpm electrode is promising, as the higher voltage required for complete activation of Li_2O could be detrimental to cell performance by overcharging the cathode and damaging the CEI [32,33].
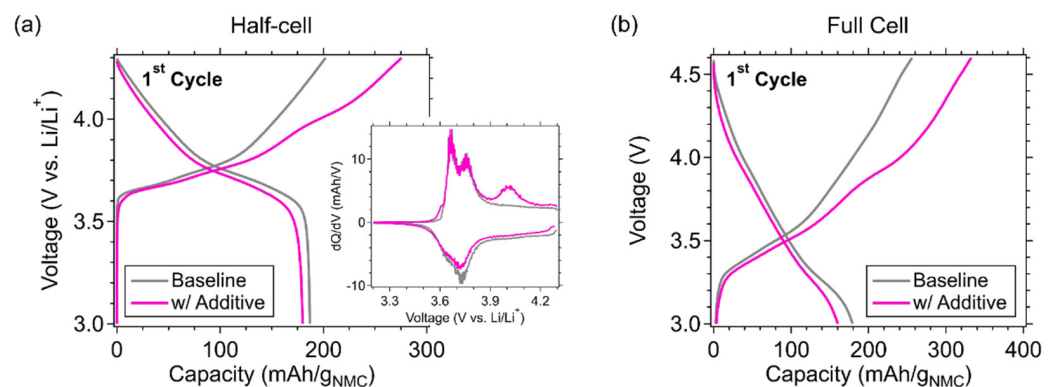

Figure 2. (**a**) Half-cell and (**b**) full-cell profiles of the baseline and the additive $Li_2O + Co_3O_4$ @1100 rpm containing electrodes during the first cycle. Half cells and full cells were charged at a C/20 rate up to 4.3 and 4.6 V, respectively. Voltage profiles are plotted as a function of grams of NMC in the electrode, excluding the mass of additives. dQ/dV plots for half cells are shown as an inset of (**a**).

When the electrode was charged up to 4.7 V vs. Li/Li^+, the reaction of Li_2O continued and an additional capacity of 1504 mAh/g_{Li2O} was obtained, which corresponds to 793 mAh/$g_{Li2O+Co3O4}$ (Figure S3). While the higher capacity per gram of Li_2O from the

Li_2O + Co_3O_4 @1100 rpm electrode compared to that from the Li_2O + Co_3O_4 @400 rpm electrode (1504 vs. 1163 mAh/g_{Li2O} with 4.7 V charging) can be attributed to the smaller particle size, as discussed in Figure 1b, the significantly lower overpotential is surprising as there was no modification of the Co_3O_4. To further understand the source of this behavior, we performed X-ray diffraction (XRD) and XPS analyses of the Li_2O + Co_3O_4 @400 rpm and Li_2O + Co_3O_4 @1100 rpm electrodes. From the XRD spectra (Figure S4), we were not able to detect a signal from the additives likely due to their relatively low content. While the XPS spectra (Figure S5) captured the transition metal core levels (Ni 2p, Co 2p, and Mn 2p), no noticeable difference was observed, even from the Co 2p signals. Thus, the lower overpotential likely resulted from morphological rather than chemical factors. Previously, Sun et al. performed transmission electron microscopy (TEM) analysis on their Co/Li_2O nanocomposite and showed that having smaller, uniformly distributed Co in intimate contact with Li_2O is key to enhancing the additive performance [23]. Thus, milling at higher revolutions per minute not only makes the particle size smaller, but can also enhance the contact between Li_2O and Co_3O_4, leading to the lower over-potential.

The Li_2O + Co_3O_4 @1100 rpm electrode was then paired with a Si anode to test its full cell performance. The areal capacities of anode and cathode used for full cells are shown in Figure S6. The first-cycle voltage profiles of the baseline and Li_2O + Co_3O_4 @1100 rpm full cells are presented in Figure 2b, and their continued cycling results are shown in Figure S7. During the first charge, additional capacity from Li_2O was observed at voltages lower than 4 V, demonstrating the successful performance of this electrode in full-cell configuration. Up to 4.1 V in full cells, 1035 mAh/g_{Li2O} (or 546 mAh/$g_{Li2O+Co3O4}$ considering the total mass of Li_2O and Co_3O_4) of capacity was obtained from the additive. However, one notable behavior observed from both half cells and full cells was the lower capacity of Li_2O + Co_3O_4 @1100 rpm electrode in the following discharge compared to that of the baseline electrode. For example, the discharge capacity of the baseline and the Li_2O + Co_3O_4 @1100 rpm electrodes was 187 and 180 mAh/g_{NMC}, respectively, in half cells (Figure 2a), and 179 and 160 mAh/g_{NMC}, respectively, in full cells (Figure 2b). The greater difference in the discharge capacity between the two electrodes in full cells likely resulted from the higher upper cutoff voltage. When the half cells were charged up to 4.7 V (Figure S3), the discharge capacity of the baseline and Li_2O + Co_3O_4 @1100 rpm electrodes was 229 and 211 mAh/g_{NMC}, respectively, which is a larger difference (18 mAh/g_{NMC}) compared to the 4.3 V charged cells (7 mAh/g_{NMC}).

Such capacity fade was observed from all additive-containing electrodes examined in this work, regardless of the presence of Co_3O_4, indicating a general degradation mechanism induced by Li_2O. To evaluate the morphological integrity of the cycled electrodes, SEM images were obtained (Figure S8a). However, there was no noticeable change in the electrode structure. To examine the potential degradation of other cell components impacting the cell performance, the cycled electrode was retrieved and reassembled into a half cell with fresh electrolyte and Li metal (Figure S8b). However, the capacity was not recovered in this case either. These results suggested that the degradation arises from chemical changes happening to the electrode during the charge. Thus, we performed XPS analysis on the cycled electrodes to understand the source of this phenomenon.

3.3. Analysis of the Cathode Surface Chemistry

The XPS spectra of baseline and Li_2O + Co_3O_4 @1100 rpm electrodes cycled between 3.0 and 4.7 V in half cells are shown in Figure 3. The electrodes were analyzed at their discharged states. C 1s, F 1s, and P 2p core levels showed peaks associated with electrolyte decomposition products. While C 1s core-level peaks (carbon black at 284.5 eV, C–C/C–H at 284.8 eV, C–O at 286.7 eV, O–C = O at 289.0 eV, and CO_3 at 291.2 eV) [34–37] showed similar intensities, the F 1s and P 2p core-level signals were stronger from the additive-containing electrodes. For example, the Li_xPF_y species (F 1s peak at 689.0 eV and P 2p peak at 138.4 eV) [34,37], which is absent in the baseline electrode, was observed from the Li_2O +

Co_3O_4 @1100 rpm electrode. In addition, the Li_xPO_y species peak at 134.9 eV [34,37] was more intense in the $Li_2O + Co_3O_4$ @1100 rpm electrode.

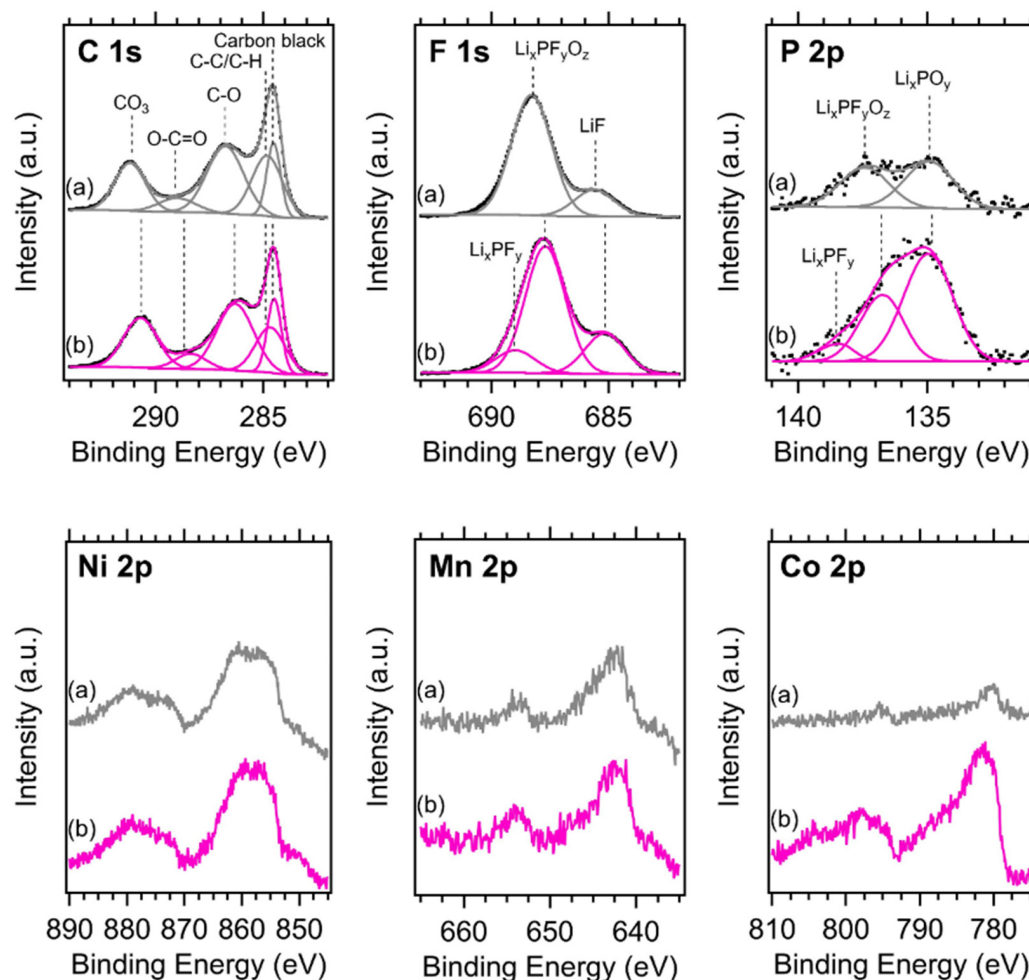**Figure 3.** XPS spectra of (**a**) baseline and (**b**) $Li_2O + Co_3O_4$ @1100 rpm electrodes cycled between 3.0 and 4.7 V. C 1s, F 1s, P 2p, Ni 2p, Mn 2p, and Co 2p core levels are shown.

These observations indicated the extensive salt decomposition taking place in the presence of additives. The formation of fluorophosphates is initiated by the hydrolysis of $LiPF_6$ and the reaction continues as the fluorophosphate species further react with additional water or solvents to form phosphates [38,39]. These reactions are accelerated by the presence of reactive oxygen species, such as peroxides and superoxides, created as intermediates during the charging of Li_2O [25,26,40]. In addition, the amount of phosphates present on the electrode is proportional to the degree of capacity fade observed after the first charge. Comparing XPS spectra readings of the $Li_2O + Co_3O_4$ @1100 rpm electrode charged up to 4.3 and 4.7 V (Figure S9), a stronger phosphate signal was observed from the 4.7 V charged electrode, which showed greater capacity fade (i.e., 18 vs. 7 mAh/g_{NMC}).

Finally, looking at the transition-metal core levels, the Ni 2p and Mn 2p spectra showed similar signals from both the baseline and $Li_2O + Co_3O_4$ @1100 rpm electrodes. On the other hand, the Co 2p spectra showed a distinctly stronger signal from the additive-containing electrode, indicating the presence of Co_3O_4 [41] after the activation of Li_2O. Interestingly, prior to cycling, the Co 2p signal from the $Li_2O + Co_3O_4$ @1100 rpm electrode was similar to that of the baseline electrode (Figure S5). Thus, Co_3O_4 may be migrating closer to the surface as Li_2O reacts and becomes converted to O_2. While it may seem that the Co_3O_4 concentrating at the surface could be impacting the utilization of NMC in the following cycles, we note that capacity fade was also observed from Li_2O-only electrodes. For

example, the discharge capacity of the Li_2O @400 rpm electrode was 196 mAh/g_{NMC} while that of the baseline electrode was 229 mAh/g_{NMC}, exhibiting a 33 mAh/g_{NMC} capacity fade (Figure S8b). Therefore, electrolyte decomposition and the creation of (fluoro)phosphate-rich CEI are the major factors damaging electrode performance.

4. Conclusions

In this work, we examined Li_2O as a potential cathode additive for providing an additional Li source in order to compensate for the first-cycle Li loss, which is a well-known problem with Si-based anodes. By utilizing an OER catalyst, Co_3O_4, to facilitate the oxidation of Li_2O and ball-milling the Co_3O_4 and Li_2O mixtures, we showed these additives can deliver 1116 mAh/g_{Li2O} or 589 mAh/$g_{Li2O+Co3O4}$ when charged up to 4.3 V vs. Li/Li$^+$. Decreasing the Li_2O particle size increased the utilization of Li_2O, and the presence of Co_3O_4 lowered the overpotential for Li_2O activation. However, the electrode suffered from degradation caused by extensive electrolyte decomposition potentially involving reactive oxygenated species created as intermediates of Li_2O oxidation. Utilizing the proposed successful, easily manufacturable additive, future work will involve (1) developing electrolytes to overcome this degradation issue, (2) designing electrodes to minimize the cell energy density loss, and (3) testing full cells with more controlled parameters (e.g., negative-to-positive (N/P) ratios, voltage range, and different anode and cathode pairs).

Supplementary Materials: The following are available online at https://www.mdpi.com/article/10.3390/app112412027/s1, SEM Images of Li_2O-containing electrodes, half-cell voltage profiles plotted as a function of areal capacity, 4.7 V charge profile of Li_2O + Co_3O_4 @1100 rpm electrode, XRD and XPS analysis of Li_2O + Co_3O_4 milled at 400 and 1100 rpm, areal capacity of full-cell electrodes, full-cell cycle performance, analysis of cycled electrodes, and impact of the upper cutoff voltage. **Figure S1.** SEM images of electrodes containing the Li_2O additives. Larger particles (~10 μm diameter) are NMC622 and the inset images show closer view of the additive particles. **Figure S2.** Half-cell voltage profiles of the additive containing and baseline electrodes during the first charge. Half-cells were charged at a C/20 rate up to 4.7 V at 30 °C. Voltage profiles are plotted as a function of mAh/cm^2. **Figure S3.** Half-cell voltage profiles of the baseline and Li_2O+Co_3O_4 @1100 rpm electrodes during the first charge at a C/20 rate up to 4.7 V plotted as a function of g of NMC in the electrode, excluding the mass of additives. **Figure S4.** XRD spectra of (a) baseline, (b) Li_2O+Co_3O_4 @400 rpm, and (c) Li_2O+Co_3O_4 @1100 rpm electrodes. Reference powder XRD patterns of NMC622 (#291468), Co_3O_4 (#9362), and Li_2O (#54368) are from the Inorganic Crystal Structure Database (ICSD). **Figure S5.** XPS spectra of (a) baseline, (b) Li_2O+Co_3O_4 @400 rpm, and (c) Li_2O+Co_3O_4 @1100 rpm electrodes. Ni 2p, Co 2p, and Mn 2p core levels are shown. **Figure S6.** Areal capacities of the (a) cathode (baseline and Li_2O+Co_3O_4 @1100 rpm electrodes) and (b) Si anode measured in half-cells. Cathodes were cycled between 3.0–4.7 V with a 0.10 mA/cm^2 current density and the Si anode was cycled between 0.05–0.75 V with a 0.15 mA/cm^2 current density. First cycle profiles are shown. **Figure S7.** Cycle performance of Baseline/Si and Li_2O+Co_3O_4 @1100 rpm/Si full cells. Charge and discharge capacity per g of NMC in the electrode, excluding the mass of additives, are plotted as a function of cycle number. Cells were cycled at C/20 rate for three cycles, then C/3 rate for 20 cycles, and finally at C/20 rate for three cycles between 3.0 and 4.6 V. **Figure S8.** (a) SEM images of Li_2O @1100 rpm electrode before (left) and after (right) cycling. (b) Voltage profiles of baseline, Li_2O @400 rpm, and reassembled Li_2O @400 rpm half-cells. The same cycle conditions were applied for all three cases. **Figure S9.** (a) First cycle half-cell voltage profiles of the baseline and Li_2O+Co_3O_4 @1100 rpm electrodes cycled between 3.0–4.3 V (left) and 3.0–4.7 V (right). (b) XPS spectra of Li_2O+Co_3O_4 @1100rpm electrodes charged up to 4.3 and 4.7 V.

Author Contributions: Data curation, Y.H., M.C.S., S.F., S.E.T., G.T. and G.M.V.; formal analysis, Y.H., N.R.N., G.M.V. and C.S.J.; funding acquisition, C.S.J.; investigation, Y.H.; methodology, Y.H. and G.M.V.; project administration, C.S.J.; resources, M.C.S., S.F., S.E.T., G.T. and G.M.V.; supervision, N.R.N.; writing—original draft, Y.H.; writing—review and editing, C.S.J. All authors have read and agreed to the published version of the manuscript.

Data Availability Statement: Data is available upon request from the corresponding authors.

Conflicts of Interest: The authors declare no conflict of interest.

References

1. Feng, K.; Li, M.; Liu, W.; Kashkooli, A.G.; Xiao, X.; Cai, M.; Chen, Z. Silicon-Based Anodes for Lithium-Ion Batteries: From Fundamentals to Practical Applications. *Small* **2018**, *14*, 1702737. [CrossRef] [PubMed]
2. Asenbauer, J.; Eisenmann, T.; Kuenzel, M.; Kazzazi, A.; Chen, Z.; Bresser, D. The success story of graphite as lithium-ion anode material—Fundamentals, remaining challenges, and recent developments including silicon (oxide) composites. *Sustain. Energy Fuels* **2020**, *4*, 5387. [CrossRef]
3. Zhang, C.; Wang, F.; Han, J.; Bai, S.; Tan, J.; Liu, J.; Li, F. Challenges and Recent Progress on Silicon-Based Anode Materials for Next-Generation Lithium-Ion Batteries. *Small Struct.* **2021**, *2*, 2100009. [CrossRef]
4. Kim, H.; Seo, M.; Park, M.H.; Cho, J. A critical size of silicon nano-anodes for lithium rechargeable batteries. *Angew. Chem. Int. Ed.* **2010**, *49*, 2146–2149. [CrossRef] [PubMed]
5. Liu, X.H.; Zhong, L.; Huang, S.; Mao, S.X.; Zhu, T.; Huang, J.Y. Size-Dependent Fracture of Silicon Nanoparticles During Lithiation. *ACS Nano* **2012**, *6*, 1522–1531. [CrossRef]
6. Holtstiege, F.; Baermann, P.; Noelle, R.; Winter, M.; Placke, T. Pre-lithiation strategies for rechargeable energy storage technologies: Concepts, promises and challenges. *Batteries* **2018**, *4*, 4. [CrossRef]
7. Jin, L.; Shen, C.; Wu, Q.; Shellikeri, A.; Zheng, J.; Zhang, C.; Zheng, J.P. Pre-Lithiation Strategies for Next-Generation Practical Lithium-Ion Batteries. *Adv. Sci.* **2021**, *8*, 2005031. [CrossRef] [PubMed]
8. Wang, F.; Wang, B.; Li, J.; Wang, B.; Zhou, Y.; Wang, D.; Liu, H.; Dou, S. Prelithiation: A Crucial Strategy for Boosting the Practical Application of Next-Generation Lithium Ion Battery. *ACS Nano* **2021**, *15*, 2197–2218. [CrossRef]
9. Shen, Y.; Zhang, J.; Pu, Y.; Wang, H.; Wang, B.; Qian, J.; Cao, Y.; Zhong, F.; Ai, X.; Yang, H. Effective Chemical Prelithiation Strategy for Building a Silicon/Sulfur Li-Ion Battery. *ACS Energy Lett.* **2019**, *4*, 1717–1724. [CrossRef]
10. Yan, M.-Y.; Li, G.; Zhang, J.; Tian, Y.-F.; Yin, Y.-X.; Zhang, C.-J.; Jiang, K.-C.; Xu, Q.; Li, H.-L.; Guo, Y.-G. Enabling SiO_x/C Anode with High Initial Coulombic Efficiency through a Chemical Pre-Lithiation Strategy for High-Energy-Density Lithium-Ion Batteries. *ACS Appl. Mater. Interfaces* **2020**, *12*, 27202–27209. [CrossRef] [PubMed]
11. Liu, N.; Hu, L.; McDowell, M.T.; Jackson, A.; Cui, Y. Prelithiated Silicon Nanowires as an Anode for Lithium Ion Batteries. *ACS Nano* **2011**, *5*, 6487–6493. [CrossRef]
12. Kim, K.H.; Shon, J.; Jeong, H.; Park, H.; Lim, S.J.; Heo, J.S. Improving the cyclability of silicon anodes for lithium-ion batteries using a simple pre-lithiation method. *J. Power Sources* **2020**, *459*, 228066. [CrossRef]
13. Kim, H.J.; Choi, S.; Lee, S.J.; Seo, M.W.; Lee, J.G.; Deniz, E.; Lee, Y.J.; Kim, E.K.; Choi, J.W. Controlled Prelithiation of Silicon Monoxide for High Performance Lithium-Ion Rechargeable Full Cells. *Nano Lett.* **2016**, *16*, 282–288. [CrossRef] [PubMed]
14. Overhoff, G.M.; Nolle, R.; Siozios, V.; Winter, M.; Placke, T. A Thorough Analysis of Two Different Pre-Lithiation Techniques for Silicon/Carbon Negative Electrodes in Lithium Ion Batteries. *Batter. Supercaps* **2021**, *4*, 1163–1174. [CrossRef]
15. Peramunage, D.; Abraham, K.M. Preparation and electrochemical characterization of overlithiated spinel $LiMn_2O_4$. *J. Electrochem. Soc.* **1998**, *14*, 1131–1136. [CrossRef]
16. Dose, W.M.; Kim, S.; Liu, Q.; Trask, S.E.; Dunlop, A.R.; Ren, Y.; Zhang, Z.; Fister, T.T.; Johnson, C.S. Dual functionality of over-lithiated NMC for high energy silicon-based lithium-ion batteries. *J. Mater. Chem. A* **2021**, *9*, 12818–12829. [CrossRef]
17. Park, K.; Yu, B.C.; Goodenough, J.B. Li3N as a Cathode Additive for High-Energy-Density Lithium-Ion Batteries. *Adv. Energy Mater.* **2016**, *6*, 1502534. [CrossRef]
18. Sun, Y.; Li, Y.; Sun, J.; Li, Y.; Pei, A.; Cui, Y. Stabilized Li3N for efficient battery cathode prelithiation. *Energy Storage Mater.* **2017**, *6*, 119–124. [CrossRef]
19. Zhang, L.; Dose, W.M.; Vu, A.D.; Johnson, C.S.; Lu, W. Mitigating the initial capacity loss and improving the cycling stability of silicon monoxide using Li_5FeO_4. *J. Power Sources* **2018**, *400*, 549–555. [CrossRef]

20. Dose, W.M.; Villa, C.; Hu, X.; Dunlop, A.R.; Piernas-Muñoz, M.J.; Maroni, V.A.; Trask, S.E.; Bloom, I.; Dravid, V.; Johnson, C.S. Beneficial Effect of Li5FeO4 Lithium Source for Li-Ion Batteries with a Layered NMC Cathode and Si Anode. *J. Electrochem. Soc.* **2020**, *167*, 160543. [CrossRef]

21. Sun, Y.; Lee, H.W.; Seh, Z.W.; Zheng, G.; Sun, J.; Li, Y.; Cui, Y. Lithium Sulfide/Metal Nanocomposite as a High-Capacity Cathode Prelithiation Material. *Adv. Energy Mater.* **2016**, *6*, 1600154. [CrossRef]

22. Liu, Z.; Ma, S.; Mu, X.; Li, R.; Yin, G.; Zuo, P. A Scalable Cathode Chemical Prelithiation Strategy for Advanced Silicon-Based Lithium Ion Full Batteries. *ACS Appl. Mater. Interfaces* **2021**, *13*, 11985–11994. [CrossRef]

23. Sun, Y.; Lee, H.-W.; Seh, Z.W.; Liu, N.; Sun, J.; Li, Y.; Cui, Y. High-capacity battery cathode prelithiation to offset initial lithium loss. *Nat. Energy* **2016**, *1*, 15008. [CrossRef]

24. Abouimrane, A.; Cui, Y.; Chen, Z.; Belharouak, I.; Yahia, H.B.; Wu, H.; Assary, R.; Curtiss, L.A.; Amine, K. Enabling high energy density Li-ion batteries through Li$_2$O activation. *Nano Energy* **2016**, *27*, 196–201. [CrossRef]

25. Qiao, Y.; Yang, H.; Chang, Z.; Deng, H.; Li, X.; Zhou, H. A high-energy-density and long-life initial-anode-free lithium battery enabled by a Li$_2$O sacrificial agent. *Nat. Energy* **2021**, *6*, 653–662. [CrossRef]

26. Liu, T.; Vivek, J.P.; Zhao, E.W.; Lei, J.; Garcia-Araez, N.; Grey, C.P. Current Challenges and Routes Forward for Nonaqueous Lithium-Air Batteries. *Chem. Rev.* **2020**, *120*, 6558–6625. [CrossRef]

27. Ma, Z.; Yuan, X.; Li, L.; Ma, Z.-F.; Wilkinson, D.P.; Zhang, L.; Zhang, J. A review of cathode materials and structures for rechargeable lithium—Air batteries. *Energy Environ. Sci.* **2015**, *8*, 2144–2198. [CrossRef]

28. Bhatt, M.D.; Geaney, H.; Nolan, M.; O'Dwyer, C. Key scientific challenges in current rechargeable non-aqueous Li–O$_2$ batteries: Experiment and theory. *Phys. Chem. Chem. Phys.* **2014**, *16*, 12093–12130. [CrossRef]

29. Wood, K.N.; Teeter, G. XPS on Li-Battery-Related Compounds: Analysis of Inorganic SEI Phases and a Methodology for Charge Correction. *ACS Appl. Energy Mater.* **2018**, *1*, 4493–4504. [CrossRef]

30. Kim, K.S.; Park, Y.J. Catalytic properties of Co$_3$O$_4$ nanoparticles for rechargeable Li/air batteries. *Nanoscale Res. Lett.* **2012**, *7*, 1–6.

31. Lu, J.; Dey, S.; Temprano, I.; Jin, Y.; Xu, C.; Shao, Y.; Grey, C.P. Co$_3$O$_4$-Catalyzed LiOH Chemistry in Li–O$_2$ Batteries. *ACS Energy Lett.* **2020**, *5*, 3681–3691. [CrossRef]

32. Sharifi-Asl, S.; Lu, J.; Amine, K.; Shahbazian-Yassar, R. Oxygen release degradation in Li-ion battery cathode materials: Mechanisms and mitigating approaches. *Adv. Energy Mater.* **2019**, *9*, 1900551. [CrossRef]

33. Wang, Q.; Shen, C.-H.; Shen, S.-Y.; Xu, Y.-F.; Shi, C.-G.; Huang, L.; Li, J.-T.; Sun, S.-G. Origin of structural evolution in capacity degradation for overcharged NMC622 via operando coupled investigation. *ACS Appl. Mater. Interfaces* **2017**, *9*, 24731–24742. [CrossRef]

34. Ha, Y.; Harvey, S.P.; Teeter, G.; Colclasure, A.M.; Trask, S.E.; Jansen, A.N.; Burrell, A.; Park, K. Long-term cyclability of Li$_4$Ti$_5$O$_{12}$/LiMn$_2$O$_4$ cells using carbonate-based electrolytes for behind-the-meter storage applications. *Energy Storage Mater.* **2021**, *38*, 581–589. [CrossRef]

35. Bryngelsson, H.; Stjerndahl, M.; Gustafsson, T.; Edstroem, K. How dynamic is the SEI? *J. Power Sources* **2007**, *174*, 970–975. [CrossRef]

36. Dedryvere, R.; Gireaud, L.; Grugeon, S.; Laruelle, S.; Tarascon, J.M.; Gonbeau, D. Characterization of Lithium Alkyl Carbonates by X-ray Photoelectron Spectroscopy: Experimental and Theoretical Study. *J. Phys. Chem. B* **2005**, *109*, 15868–15875. [CrossRef]

37. Tatara, R.; Karayaylali, P.; Yu, Y.; Zhang, Y.; Giordano, L.; Maglia, F.; Jung, R.; Schmidt, J.P.; Lund, I.; Shao-Horn, Y. The effect of electrode-electrolyte interface on the electrochemical impedance spectra for positive electrode in Li-ion battery. *J. Electrochem. Soc.* **2019**, *166*, A5090–A5098. [CrossRef]

38. Gruetzke, M.; Kraft, V.; Hoffmann, B.; Klamor, S.; Diekmann, J.; Kwade, A.; Winter, M.; Nowak, S. Aging investigations of a lithium-ion battery electrolyte from a field-tested hybrid electric vehicle. *J. Power Sources* **2015**, *273*, 83–88. [CrossRef]

39. Henschel, J.; Peschel, C.; Klein, S.; Horsthemke, F.; Winter, M.; Nowak, S. Clarification of Decomposition Pathways in a State-of-the-Art Lithium Ion Battery Electrolyte through 13C-Labeling of Electrolyte Components. *Angew. Chem. Int. Ed.* **2020**, *59*, 6128–6137. [CrossRef]

40. Lai, J.; Xing, Y.; Chen, N.; Li, L.; Wu, F.; Chen, R. Electrolytes for rechargeable lithium—Air batteries. *Angew. Chem. Int. Ed.* **2020**, *59*, 2974–2997. [CrossRef]

41. Biesinger, M.C.; Payne, B.P.; Grosvenor, A.P.; Lau, L.W.M.; Gerson, A.R.; Smart, R.S.C. Resolving surface chemical states in XPS analysis of first row transition metals, oxides and hydroxides: Cr, Mn, Fe, Co and Ni. *Appl. Surf. Sci.* **2011**, *257*, 2717–2730. [CrossRef]